Post-Print

This is the accepted version of:

The final publication is available at https://doi.org/10.1017/jfm.2022.712

Access to the published version may require subscription.

When citing this work, cite the original published paper.

An almost subharmonic instability in the flow past rectangular cylinders

Alessandro Chiarini, Maurizio Quadrio and Franco Auteri†

Dipartimento di Scienze e Tecnologie Aerospaziali, Politecnico di Milano, via La Masa 34, 20156 Milano, Italy

The three-dimensional instability of the flow past a 5:1 rectangular cylinder is investigated via Floquet analysis and direct numerical simulations. A quasi subharmonic (QS) unstable mode is detected, marking an important difference with the flow past bodies with lower aspect ratio and/or with smooth leading edge. The QS mode becomes unstable at a Reynolds number (based on the cylinder thickness and free-stream velocity) of $Re \approx 480$; its spanwise wavelength is approximately three times the cylinder thickness. The structural sensitivity locates the wavemaker region over the longitudinal sides of the cylinder, indicating that the instability is triggered by the mutual inviscid interaction of vortices generated by the leading-edge shear layer.

Key words: Floquet analysis, bluff bodies, rectangular cylinders

1. Introduction

The flow around bluff bodies with sharp corners is frequently encountered in practical applications, especially in the field of vortex-induced oscillations (Williamson & Govardhan 2008), and is also of importance for fundamental research. The flow is complex, with massive separations at the corners producing shear layers that may reattach, several recirculating regions that may foster different instabilities, and a large downstream wake.

The rectangular cylinder is the prototype of such bodies. Varying its aspect ratio $Æ$, i.e. the ratio between the length L and the cross-stream dimension D, a set of blunt bodies is obtained, ranging from the flat plate perpendicular to the incoming flow ($Æ = 0$), to the square cylinder ($Æ = 1$) and to the flat plate parallel to the flow ($Æ \to \infty$). Already at moderate Reynolds numbers, the flow dynamics depends on the aspect ratio. For small $Æ$, i.e. $Æ \leqslant 1$, two shear layers separate from the leading-edge (LE) corners and roll up to create the classic von Kármán vortex street. In contrast, for intermediate $Æ$, i.e. $1 < Æ \leqslant 3$, the shear layers separating from the LE reattach intermittently over the

† Email address for correspondence: franco.auteri@polimi.it

lateral sides of the cylinder. For large $Æ$, the shear layers reattach permanently and the flow eventually separates at the trailing-edge (TE) corners, leading to vortex shedding from both LE and TE. When the Reynolds number Re (defined with the unperturbed velocity U_∞ and the thickness D) is large enough, say $Re \geqslant 300$, the two sheddings lock to the same frequency, leading to an almost stepwise dependence of the Strouhal number St, i.e. the shedding frequency made dimensionless with U_∞ and L, on the aspect ratio (Okajima 1982; Nakamura *et al.* 1991; Ozono *et al.* 1992; Mills *et al.* 1995). The number n of LE vortices simultaneously present over the cylinder side increases in a quantized manner with $Æ$, being for example $n = 1$ for $Æ = 4$, $n = 2$ for $Æ = 7$ and $n = 3$ for $Æ = 11$. In a previous work (Chiarini *et al.* 2022) we have found that the flow assumes different configurations depending on the prevalence of either shedding. When the overall frequency is selected by the LE vortices $St \approx n{\cdot}U_c$, $U_c \approx 0.55U_\infty$ being the mean convection velocity of the LE vortices (Mills *et al.* 2002; Tan *et al.* 2004), as the shedding frequency locks to the passing frequency of the LE vortices over the TE. In contrast, when the TE shedding dominates, the flow matches the shedding frequency of elongated bodies with rounded LE which do not produce shedding. When allowed by the phasing of the LE vortices, the flow preferentially assumes the latter configuration.

The primary and secondary instability of the flow past a square cylinder has been studied by several scholars. The onset of the primary, two-dimensional instability closely resembles that of the circular cylinder, where the flow undergoes a Hopf bifurcation, albeit at a slightly lower Reynolds number (Sohankar *et al.* 1999; Saha *et al.* 2000; Jiang & Cheng 2018). A Floquet analysis was used by Robichaux *et al.* (1999), Blackburn & Lopez (2003) and Blackburn & Sheard (2010) to study the secondary, three-dimensional instability: again, it was found to be quite similar to the circular cylinder case, with unstable synchronous A and B Floquet modes. At larger Re, a further unstable quasi-periodic mode, called QP, was identified for circular and square cylinders (Blackburn & Lopez 2003; Blackburn *et al.* 2005). Modes A and B were also observed via direct numerical simulations by Jiang *et al.* (2018), who remarked that the instability of mode A is hysteretic. Sheard *et al.* (2009) and Sheard (2011) studied how the angle of incidence affects the unstable modes: mode A is the most unstable one at small and large incidences, while a subharmonic mode, called C, is the most unstable at intermediate angles. Park & Yang (2016) studied how instabilities change when the sharp edges become rounded and the square shape approaches the circular one. For the three-dimensional instability, they found that rounding does not alter the sequence at which the three modes become unstable, yet their critical Reynolds number, i.e. the Reynolds number evaluated at their first onset, is affected because of changes of the periodic base flow.

The instabilities of the flow past rectangular cylinders with $Æ \neq 1$ have received less attention, perhaps under the assumption that no substantial changes from the square cylinder are to be expected. However, studying the primary instability for $0.25 \leqslant Æ \leqslant 30$, Chiarini *et al.* (2021*b*) recently observed that already at low Reynolds numbers some characteristics of the flow instabilities do change with the aspect ratio. They found that the primary instability is invariably the result of a Hopf bifurcation, but that the increase of $Æ$ consistently delays its first onset, with the critical Reynolds number going from $Re \approx 34$ for $Æ = 0.25$ to $Re \approx 140$ for $Æ = 30$. Moreover, the stabilising/destabilising effect of rounded LE and/or TE corners was shown to depend on $Æ$, being related to different

modifications of the base flow with respect to the sharp-corner configuration. Choi & Yang (2014) studied the secondary instability of the flow past rectangular cylinders ranging from a flat plate normal to the flow ($\mathcal{R} \to 0$) to the square cylinder ($\mathcal{R} = 1$): the decrease of $\mathcal{R}$ was found to stabilise modes A, B and QP, while two other (synchronous and quasi-periodic) modes, called A2 and QP2, become unstable (see also Thompson *et al.* 2006). Chaurasia & Thompson (2011) and Huang *et al.* (2017) studied the flow past a semi-indefinite plate of finite thickness, i.e. $\mathcal{R} \to \infty$. With a Floquet stability analysis they found that the vortices arising from the Kelvin–Helmholtz instability of the LE shear layer become globally unstable to three-dimensional perturbations at $Re \approx 380$, and that the unstable mode is subharmonic. Ryan *et al.* (2005) observed that the onset of the three-dimensional instability for elongated cylinders depends on the aspect ratio even in the simplified case without LE shedding. They investigated the transition to three-dimensional flow for cylinders with elliptic LE and square TE using both Floquet analysis and three-dimensional direct numerical simulations. They found mode A and two new modes as well, called B′ and S′ in analogy with the circular and square cylinder cases. They observed that, for small $\mathcal{R}$, i.e. $\mathcal{R} \leqslant 7.5$, the first mode which becomes unstable is mode A while, for larger $\mathcal{R}$, the first unstable mode is B′. For elongated rectangular cylinders with sharp LE corners the scenario is likely to be further complicated, as vortex shedding occurs from both LE and TE. However, the three-dimensional instability of the flow past elongated rectangular cylinders has not been properly addressed yet. To the best of our knowledge, only Hourigan *et al.* (2001) performed direct numerical simulations for rectangular cylinders with $\mathcal{R} = 6, 10$ and 13 at $Re = 350 - 400$ to describe the structure of the three-dimensional flow in the laminar regime. For the two largest $\mathcal{R}$, they observed hairpin-like structures arranged in a staggered manner on both sides of the cylinder, closely resembling those classified as pattern B in Sasaki & Kiya (1991) for a flat plate parallel to the flow.

The rectangular cylinder with $\mathcal{R} = 5$ defines the Benchmark of the Aerodynamics of a Rectangular 5:1 Cylinder or BARC (see `https://www.aniv-iawe.org/barc-docs/`), which aims at characterising the flow and setting the standards for simulations and experiments in the turbulent regime. At large Reynolds numbers, the small-scale velocity fluctuations associated with the turbulent motions coexist and interact with the large-scale motions due to the flow instabilities, giving rise to a self-sustaining cycle (Cimarelli *et al.* 2018; Moore *et al.* 2019; Chiarini *et al.* 2021*a*). Hence, the study of the flow instabilities at low Reynolds numbers and the comprehension of their triggering mechanisms is crucial also to understand the complex and multiscale flow dynamics in the turbulent regime.

The present study addresses the three-dimensional instability of the flow past a rectangular cylinder with $\mathcal{R} = 5$ via Floquet analysis and three-dimensional direct numerical simulations. An unstable mode of almost subharmonic nature, undetected for other bluff bodies, will be characterised, and a physical interpretation of the triggering mechanism will be proposed. The paper is organised as follows. After this introduction, a brief description of the mathematical formulation and of the numerical methods are provided in §2. Then the two-dimensional periodic base flow is detailed in §3. The unstable mode resulting from both the Floquet analysis and the three-dimensional direct numerical simulation is characterised in §4. Section §5 describes the onset of a second two-dimensional instability of the two-dimensional base flow at larger Re. Finally, a concluding discussion is
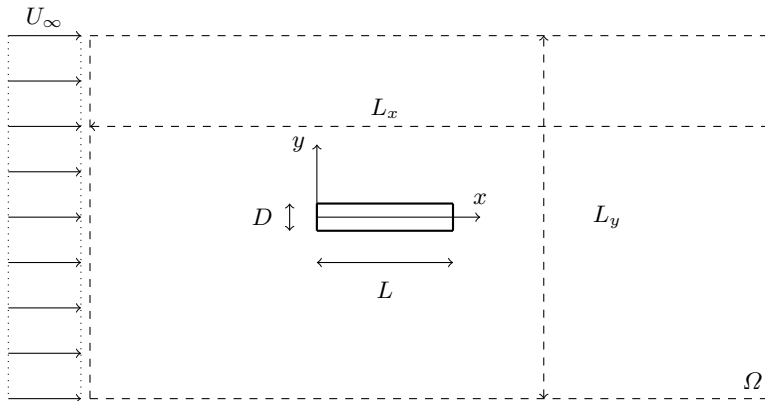
Figure 1: Sketch of the computational domain Ω containing the rectangular cylinder, and the reference system.

presented in §6. Appendix A concludes the paper and addresses the dependence of the results on the domain size and grid resolution.

2. Problem setup, mathematical formulation and discretisation

2.1. Flow configuration

The incompressible flow past a two-dimensional rectangular cylinder with aspect ratio $\mathit{R} \equiv L/D = 5$ is considered, with L and D being the cylinder length and thickness. Figure 1 shows the geometry, the reference system and the notation. A Cartesian coordinate system is used, with origin at the leading edge of the cylinder, with the x axis aligned with the flow direction and the y axis denoting the cross-stream direction. The cylinder is placed in a uniform stream with velocity U_∞. The computational domain Ω is rectangular with dimensions L_x and L_y. The Reynolds number, based on the undisturbed velocity U_∞ and on the cylinder thickness, is defined as $Re = U_\infty D/\nu$ where ν is the kinematic viscosity. The flow is governed by the incompressible Navier–Stokes equations written in dimensionless form:

$$\begin{cases} \dfrac{\partial \boldsymbol{U}}{\partial t} + \boldsymbol{U} \cdot \boldsymbol{\nabla} \boldsymbol{U} = -\boldsymbol{\nabla} P + \dfrac{1}{Re} \Delta \boldsymbol{U}, \\ \boldsymbol{\nabla} \cdot \boldsymbol{U} = 0, \end{cases} \tag{2.1}$$

where $\boldsymbol{U}$ is the velocity vector of components (U, V, W) and P is the reduced pressure. No-slip and no-penetration boundary conditions are applied on the cylinder surface, whereas an undisturbed uniform velocity is assumed in the far field. The outflow boundary condition $P\boldsymbol{n} - \frac{1}{Re}\boldsymbol{\nabla} \boldsymbol{U} \cdot \boldsymbol{n} = 0$, where $\boldsymbol{n}$ is the normal vector, is used at the outflow boundary.

2.2. Secondary instability: Floquet analysis

When the value of the Reynolds number is above the critical value Re_{c1} of the Hopf bifurcation for the primary instability, but below the critical value Re_{c2} for the secondary instability, the flow is periodic and two-dimensional. The Floquet theory is used to study the linear stability analysis of the two-dimensional and time-periodic base flow to three-dimensional disturbances. As long as $Re_{c1} \leqslant$

$Re \leqslant Re_{c2}$, the flow field $\{\boldsymbol{U}, P\}$ is written as the sum of a two-dimensional base flow $\{\boldsymbol{U}_b, P_b\}$ which is periodic with period T and an unsteady three-dimensional perturbation with small amplitude ϵ:

$$
\begin{aligned}
\boldsymbol{U}(x,y,z,t) &= \boldsymbol{U}_b(x,y,t) + \epsilon \frac{1}{\sqrt{2\pi}} \int_{-\infty}^{\infty} \boldsymbol{u}(x,y,k,t) \mathrm{e}^{ikz} dk, \\
P(x,y,z,t) &= P_b(x,y,t) + \epsilon \frac{1}{\sqrt{2\pi}} \int_{-\infty}^{\infty} p(x,y,k,t) \mathrm{e}^{ikz} dk,
\end{aligned}
\tag{2.2}
$$

where i is the imaginary unit, $\boldsymbol{u}$ and p indicate the Fourier transform of the velocity and pressure disturbances in the homogeneous spanwise direction z, and k is the corresponding wavenumber.

Introducing the decompositions (2.2) into the governing equations (2.1), the two-dimensional, base-flow equation is obtained at order ϵ^0, while the eigenproblem describing the linear evolution of the three-dimensional disturbances is obtained at order ϵ. By applying the Fourier transform in z, the Linearised Navier–Stokes equations (LNSEs) read for each k:

$$
\begin{cases}
\dfrac{\partial \boldsymbol{u}}{\partial t} + \boldsymbol{L}_k\{\boldsymbol{U}_b, Re\}\boldsymbol{u} + \boldsymbol{\nabla}_k p = 0, \\
\boldsymbol{\nabla}_k \cdot \boldsymbol{u} = 0,
\end{cases}
\tag{2.3}
$$

where $\boldsymbol{\nabla}_k \equiv (\partial/\partial x, \partial/\partial y, ik)$ is the Fourier-transformed gradient operator, and $\boldsymbol{L}_k$ is the Fourier-transformed linearised Navier–Stokes operator:

$$
\boldsymbol{L}_k\{\boldsymbol{U}_b, Re\}\boldsymbol{u} = \boldsymbol{U}_b \cdot \boldsymbol{\nabla}_k \boldsymbol{u} + \boldsymbol{u} \cdot \boldsymbol{\nabla}_k \boldsymbol{U}_b - \frac{1}{Re}\Delta_k \boldsymbol{u},
\tag{2.4}
$$

in which $\Delta_k \equiv \boldsymbol{\nabla}_k \cdot \boldsymbol{\nabla}_k$ is the Fourier-transformed Laplacian operator. According to the Floquet theory, we assume the following functional form for the perturbation field $\{\boldsymbol{u}, p\}$:

$$
\begin{aligned}
\boldsymbol{u}(x,y,k,t) &= \hat{\boldsymbol{u}}(x,y,k,t)\mathrm{e}^{\sigma t}, \\
p(x,y,k,t) &= \hat{p}(x,y,k,t)\mathrm{e}^{\sigma t},
\end{aligned}
\tag{2.5}
$$

where σ is the Floquet exponent and $\{\hat{\boldsymbol{u}}, \hat{p}\}$ is the Floquet mode associated with σ and k, possessing the same periodicity of the base flow:

$$
\{\hat{\boldsymbol{u}}, \hat{p}\}(x,y,k,t+T) = \{\hat{\boldsymbol{u}}, \hat{p}\}(x,y,k,t).
\tag{2.6}
$$

These modes can be obtained by a Krylov subspace method together with the Arnoldi iteration algorithm (Barkley & Henderson 1996). The stability of the system is determined by the sign of the real part $\Re(\sigma)$ of the Floquet exponent or, equivalently, by the modulus of the Floquet multiplier $\mu = \mathrm{e}^{\sigma T}$. If all $\Re(\sigma) < 0$, or $|\mu| < 1$, the perturbations decay and the flow remains two-dimensional; otherwise, if at least one exponent exists with $\Re(\sigma) > 0$, or $|\mu| > 1$, the perturbations grow exponentially and the flow becomes three-dimensional if $k \neq 0$.

2.3. *Structural sensitivity*

A better understanding of the instability can be obtained through the structural sensitivity, introduced by Giannetti & Luchini (2007) for the primary instability and then extended by Giannetti *et al.* (2010) to the secondary instability. It is based on direct and adjoint modes.
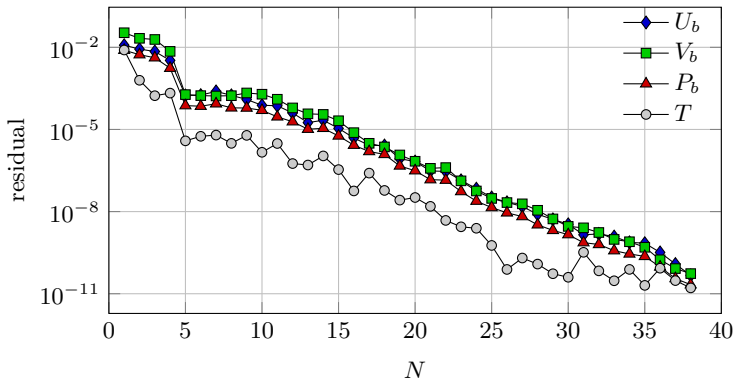
Figure 2: Convergence of the base flow to its periodic limit cycle at $Re = 500$.
Decrease of the residuals with the number N of shedding cycles.

The adjoint LNSEs are:

$$\begin{cases} -\dfrac{\partial \boldsymbol{f}^+}{\partial t} + \mathrm{L}_k^+\{\boldsymbol{U}_b, Re\}\boldsymbol{f}^+ - \boldsymbol{\nabla}_k m^+ = 0, \\ \boldsymbol{\nabla}_k \cdot \boldsymbol{f}^+ = 0, \end{cases} \tag{2.7}$$

where $\mathrm{L}_k^+\{\boldsymbol{U}_b, Re\}$ is the Fourier-transformed adjoint linearised Navier–Stokes operator:

$$\mathrm{L}_k^+\{\boldsymbol{U}_b, Re\}\boldsymbol{f}^+ = -\left(\boldsymbol{U}_b \cdot \boldsymbol{\nabla}_k\right)\boldsymbol{f}^+ + \left(\boldsymbol{\nabla}_k \boldsymbol{U}_b\right) \cdot \boldsymbol{f}^+ - \frac{1}{Re}\Delta_k \boldsymbol{f}^+. \tag{2.8}$$

The adjoint solution $\{\boldsymbol{f}^+, m^+\}$ provides the receptivity of the modes to an external forcing, so that direct and adjoint perturbation modes highlight the regions of maximum perturbation and maximum receptivity. The structural sensitivity tensor S puts these pieces of information together, and identifies the so-called wave-maker region (Monkewitz *et al.* 1993), i.e. the region where the instability takes place. It is defined as:

$$S(x, y, k) = \frac{\int_t^{t+T} \hat{\boldsymbol{f}}^+(x, y, k, t)\hat{\boldsymbol{u}}(x, y, k, t) \, dt}{\int_t^{t+T} \int_\Omega \hat{\boldsymbol{f}}^+ \cdot \hat{\boldsymbol{u}} \, d\Omega \, dt}. \tag{2.9}$$

The instability mechanism may be elucidated by inspecting the different components of S. However, as shown by Giannetti *et al.* (2010), it is easier to choose a norm $||\cdot||$ and to extract information from S by plotting $||S(x, y, k)||$ at each point of the space. Note that, while S provides information which is averaged over the period T, it may be meaningful to consider the instantaneous sensitivity tensor $I(x, y, k, t)$ defined as:

$$I(x, y, k, t) = \frac{\hat{\boldsymbol{f}}^+(x, y, k, t)\hat{\boldsymbol{u}}(x, y, k, t)}{\int_t^{t+T} \int_\Omega \hat{\boldsymbol{f}}^+ \cdot \hat{\boldsymbol{u}} \, d\Omega \, dt}. \tag{2.10}$$

2.4. Numerical methods

The two-dimensional periodic base flow is computed by integrating in time the discretised two-dimensional version of the Navier–Stokes equations (2.1). The time integration employs an explicit third-order, low-storage Runge–Kutta

method for the nonlinear term, combined with an implicit second-order Crank–Nicolson scheme (Rai & Moin 1991) for the linear terms. The spatial discretisation uses finite elements, with quadratic elements for velocity and linear elements for pressure to satisfy the LBB condition (Brezzi 1974). Simulations are implemented in the non-commercial software FreeFem++ (Hecht 2012). The BoostConv algorithm, an iterative algorithm inspired by the Krylov subspace methods, is used to accelerate the convergence of the simulations to the periodic limit cycle (Citro *et al.* 2017). Figure 2 shows the decrease of residuals, defined as the absolute value of the largest difference over the computational domain between variables at t and $t+T$. At $Re = 500$, velocity and pressure residuals decrease fast, as well as that of period T. An almost exponential decrease is observed, with residuals reaching 10^{-10} after 38 shedding periods, and the base flow is verified to satisfy the required spatio-temporal symmetries

$$
\begin{aligned}
U_b(x, y, t) &= U_b(x, -y, t + T/2), \\
V_b(x, y, t) &= -V_b(x, -y, t + T/2), \\
P_b(x, y, t) &= P_b(x, -y, t + T/2)
\end{aligned}
\tag{2.11}
$$

within the same threshold.

The numerical method used for the Floquet analysis is similar to that used in other references, for example Barkley & Henderson (1996); Jallas *et al.* (2017). If $\boldsymbol{u}_k(t_0)$ is the velocity perturbation with wavenumber k at time t_0, its evolution after one period can be written using the linearised Poicaré map P_k as:

$$
\boldsymbol{u}_k(t_0 + T) = P_k \boldsymbol{u}_k(t_0). \tag{2.12}
$$

The eigenvalues and eigenvectors of P_k are the Floquet multipliers μ_k and the Floquet modes $\hat{\boldsymbol{u}}_k(t_0)$ at the time t_0 of the operator L_k. We have used the Arnoldi method (Saad 2011) to compute the eigenvalues of P_k with largest modulus and the associated eigenvectors. To this purpose, the action of P_k on the perturbation $\boldsymbol{u}_k(t_0)$ is obtained by integrating equations (2.3) in time from t_0 to $t_0 + T$. The modified Gram-Schmidt algorithm is used for the orthogonalisation of the eigenvectors, and all the computed modes are normalised using their total kinetic energy. Finally, the evolution of the Floquet mode $\hat{\boldsymbol{u}}_k(t)$ over the period T is evaluated by integrating equations (2.3) in time. In doing this, the initial condition is the approximated eigenvector $\hat{\boldsymbol{u}}_k(t_0)$ previously computed; the result of the integration is then corrected by $e^{-\lambda t}$ to account for (2.5). For consistency, the time integration of the LNSEs is carried out using the same numerical scheme used for integrating the two-dimensional Navier–Stokes equations to compute the base flow. During the time integration of the LNSEs, the base flow is evaluated at each time step by the Fourier interpolation of 100 instantaneous fields stored uniformly over one period T. The same approach is used when computing the adjoint modes, but considering equations (2.7) instead of (2.3); the adjoint modes are normalised by their total kinetic energy.

The computational domain extends for $-25D \leqslant x \leqslant 50D$ in the streamwise direction and for $-20D \leqslant y \leqslant 20D$ in the cross-stream direction, corresponding to a size of $(L_x, L_y) = (75D, 40D)$. A symmetric grid with respect to the x-axis has been used, to avoid the introduction of asymmetries in the flow. The number of triangles is approximately 1.2×10^5, with 200 and 100 elements over the longitudinal and vertical sides of the cylinder, respectively. The sensitivity of the results on the domain size and grid resolution are discussed in appendix A.

For the direct problem, homogeneous Dirichlet boundary conditions are used at the inlet and at the farfield, while homogeneous Neumann boundary conditions for the velocity are used at the outflow. For the adjoint problem, instead, we have used homogeneous Dirichlet boundary conditions for the velocity at all the boundaries of the domain as in Giannetti *et al.* (2010).

The 3D direct numerical simulations have been performed using a DNS code introduced by Luchini (2016). The code solves the three-dimensional incompressible Navier–Stokes equations written in primitive variables on a staggered Cartesian grid using second-order finite differences in all directions. The momentum equations are advanced in time by a fractional-step method using a third-order Runge-Kutta scheme. The Poisson equation for the pressure is solved by an iterative SOR algorithm. The cylinder is considered with a second-order implicit immersed-boundary method, implemented in staggered variables (Luchini 2013, 2016). The unperturbed flow $(U_\infty, 0, 0)$ is imposed at the inlet and in the far field, periodic boundary conditions are used in the spanwise direction and convective outlet conditions at the outflow. This DNS code has been previously used to compute the flow past a rectangular cylinder with $\mathcal{R} = 5$ in the turbulent regime by Chiarini & Quadrio (2021).

The computational domain used for the three-dimensional simulation extends for $-30D \leqslant x \leqslant 80D$, $-25D \leqslant y \leqslant 25D$ and $0 \leqslant z \leqslant 2\pi D$, corresponding to a size of $(L_x, L_y, L_z) = (110D, 50D, 2\pi D)$; z denotes the spanwise periodic direction. The cylinder is placed at $0 \leqslant x \leqslant 5D$ and $-0.5D \leqslant y \leqslant 0.5D$. The domain is discretised with $N_x \approx 1072$, $N_y \approx 590$ and $N_z \approx 200$ points in the three directions, for a total of about 130 million points. Their distribution is homogeneous in the spanwise direction, whereas a geometric progression is adopted in the streamwise and vertical directions to properly refine the grid near the corners of the body. The number of points along the longitudinal and vertical sides of the cylinder is respectively 270 and 170. The cell size near the corners is approximately $\Delta x = \Delta y \approx 0.005$. Hereinafter, if not otherwise indicated, all variables are in dimensionless form with D as length scale, U_∞ as velocity scale and D/U_∞ as time scale.

3. Base flow

To characterise the two-dimensional periodic base flow, the beginning of each cycle is identified by the condition $C_\ell = 0$ and $\partial C_\ell / \partial t > 0$, where C_ℓ is the lift coefficient, i.e. the vertical component of the aerodynamic force, made dimensionless with $0.5\rho U_\infty^2 D$. The flow separates at the LE and reattaches at a point x_r along the cylinder side; the recirculating region on each side of the cylinder periodically enlarges and shrinks while LE vortices are being shed. This is described by the evolution in time of the reattachment point x_r over one shedding period, shown in figure 3 for $Re = 550$. The length of the recirculating region reaches its minimum, $x_r \approx 2.6$, after the shedding of a new LE vortex at $t/T \approx 0.85$. Then x_r linearly increases until the maximum $x_r \approx 4.25$ is reached, to shrink again as a new vortex is shed downstream.

Figure 4 shows streamlines and the vorticity (ω_z) colour map at four instants within one half of the shedding period (the spatio-temporal symmetry allows one to reconstruct the base flow over the complete period). The stagnation points are marked with symbols. Grey diamonds are used for the elliptical stagnation points corresponding to a local maximum or minimum of the stream function
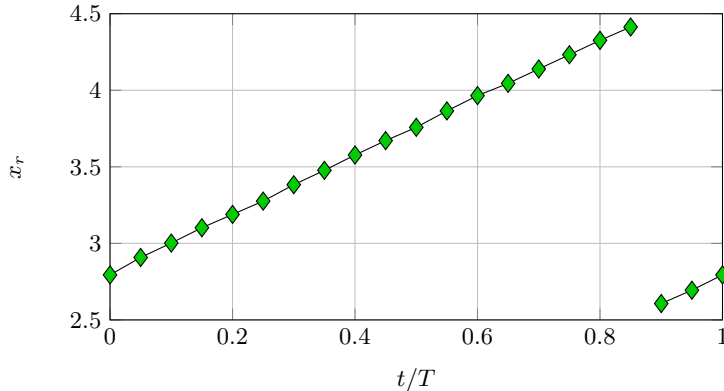
Figure 3: Position of the reattachment point x_r on the top surface along the period as a function of t/T for $Re = 550$.
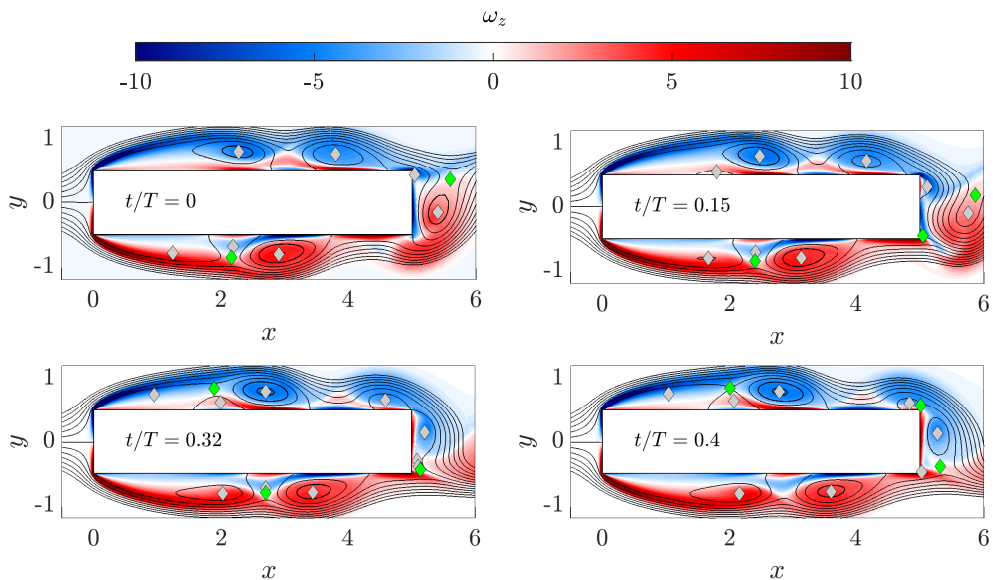

Figure 4: Snapshots of the base flow at $Re = 550$, taken at four different instants along the period. Streamlines are superimposed to the ω_z vorticity map (blue and red are clockwise and counterclockwise vorticity, respectively). Grey/green diamonds indicate elliptical/hyperbolic stagnation points.

ψ, defined as $\nabla^2 \psi = -\omega_z$; green diamonds indicate hyperbolic stagnation points corresponding to saddle points of ψ. Within the large recirculating region over the cylinder side, the reverse boundary layer periodically separates, owing to the adverse pressure gradient, and produces a smaller secondary counter-rotating recirculation region near the body. The size of this recirculating region increases over the shedding period, until a new LE vortex is shed downstream towards the TE. As shown by Chiarini *et al.* (2022), this vortex reaches the TE in phase with the development of a new TE vortex from the same side (top right panel) and the two then coalesce before being shed in the wake (bottom panels).

The vortex splitting taking place in the main top and bottom recirculation
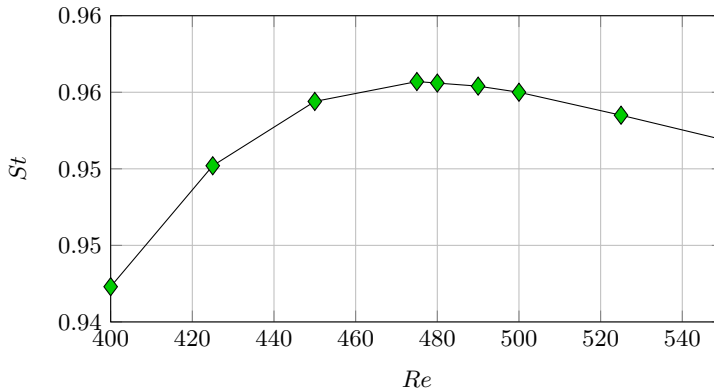
Figure 5: Dependence of St on Re.

regions and responsible of the LE vortex shedding is described following the work by Boghosian & Cassel (2016). In a two-dimensional incompressible flow, a splitting event takes place at a point within a recirculation region if and only if: (i) the point is a critical point for the streamfunction, $\partial\psi/\partial x = \partial\psi/\partial y = 0$, i.e. a stagnation point with $u = v = 0$; and (ii) the quantity Q

$$Q = \frac{\partial u}{\partial x}\frac{\partial v}{\partial y} - \frac{\partial u}{\partial y}\frac{\partial v}{\partial x}$$

evaluated at the point is negative. In other words, a hyperbolic stagnation point is required for splitting. For the top side at $t/T = 0$, shedding has just occurred and the size of the recirculation region is at its minimum. Two elliptic stagnation points (with $Q > 0$) identify the centre of rotation of the main recirculation region and the vortex just shed from it. A similar situation is observed for $t/T = 0.15$, but a new elliptic stagnation point indicates the appearance of the secondary counter-rotating recirculation. At $t/T = 0.32$ a hyperbolic stagnation point appears at $x \approx 2$, just above the secondary recirculation: at this time, vortex splitting is allowed. Shortly thereafter, the elliptical stagnation point associated with the counter-rotating region and the new hyperbolic one become closer until they collapse, and vortex splitting actually occurs. Splitting completes at $t/T \approx 0.85$, resulting in the abrupt reduction of the length of the primary recirculation shown in figure 3.

   Figure 5 shows the dependence of the Strouhal number $St = fL/U_\infty$, i.e. the shedding frequency made dimensionless with L and U_∞, on Re in the range $400 \leqslant Re \leqslant 550$. Within this range, St does not change significantly, with a maximum variation of about 1.4%. However, St increases to a maximum at $Re \approx 485$ and then monotonically decreases. Interestingly, the Re of maximum St approximately corresponds to the first onset of the three-dimensional instability, as it will be shown in the following. We also note that, for $Re \geqslant 555$, the two-dimensional base flow undergoes a further two-dimensional instability and enters a non-periodic regime where the LE and TE shedding are no longer locked to the same frequency. This is described in §5.
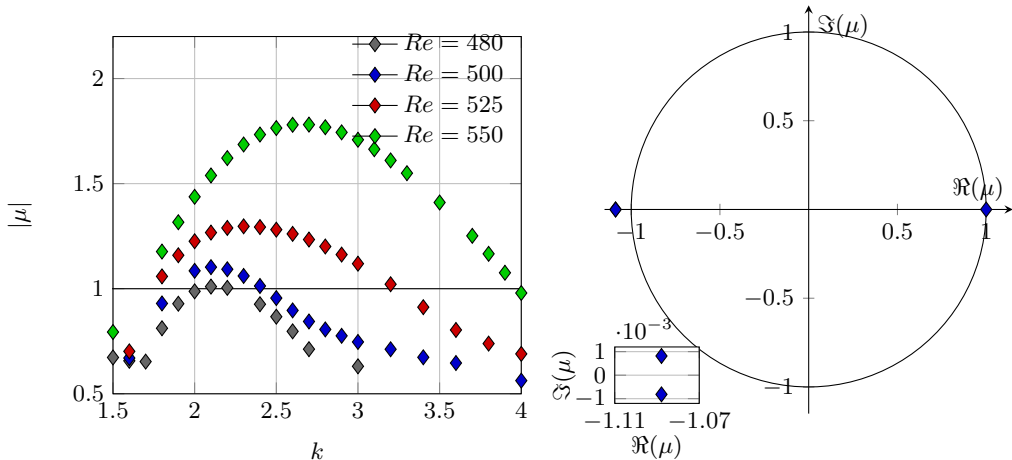
Figure 6: Left: modulus of the most unstable Floquet multiplier at
$Re = 480, 500, 525, 550$ for $1.5 \leqslant k \leqslant 4$. Right: Floquet multipliers in the
complex plane for $k = 2.1$ at $Re = 500$. The inset zooms on the unstable pair
outside the unitary circle.

4. An almost subharmonic instability

4.1. *Floquet multipliers*

Figure 6 shows the dominant Floquet multipliers for four values of Re in the
range $480 \leqslant Re \leqslant 550$. The left panel shows the magnitude of the multipliers for
wavenumbers $1.5 \leqslant k \leqslant 4$ for which they become unstable, while the right panel
plots the Floquet multipliers in the complex space for $Re = 500$ and $k = 2.1$.

A first multiplier with $|\mu| > 1$ appears for $Re = Re_{c2} \approx 480$ and $k \approx 2.1$. For
$Re > Re_{c2}$, a band of unstable wavenumbers appears. As Re increases, this band
widens and the branch moves towards slightly larger k. The right panel shows
the unstable branch to correspond to a pair of complex conjugate multipliers
with negative real part and very small imaginary part. The figure shows the
expected multiplier $\mu = (1, 0)$ associated with the time-translation symmetry of
the base flow, and highlights in the inset a pair of complex conjugate multipliers
$\mu = (-1.087, \pm 0.000816)$ outside the unit circle. This pair indicates that the
periodic two-dimensional base flow is linearly unstable to three-dimensional quasi-
subharmonic perturbations. Indeed, it corresponds to a pair of complex conjugate
eigenvalues $\sigma = 1/T \log(\mu) \approx (0.0073, \pm 0.6012)$ that denote an unstable mode
($\Re(\sigma) > 0$) with a period of $2\pi/\Im(\sigma) \approx 10.45$, which is almost twice the period
of the base flow. Hereafter we refer to this mode as mode QS.

Mode QS substantially differs from mode QP observed for the square cylinder
(Blackburn & Sheard 2010) and mode S′ observed for elongated cylinders without
LE vortex shedding (Ryan *et al.* 2005). Indeed, the wavenumber is clearly differ-
ent: the latter modes have both $k \approx 5 - 6$ instead of $k \approx 2$. More importantly,
they are quasi-periodic modes corresponding to a pair of complex conjugate
Floquet multipliers with relatively large imaginary part: Blackburn & Sheard
(2010) report $\Im(\mu) \approx 0.4$ for mode QP and we have computed $\Im(\mu) \approx 0.1$ for
mode S′ in the case of a D-shaped cylinder with $Æ = 5$ at $Re = 500$. This
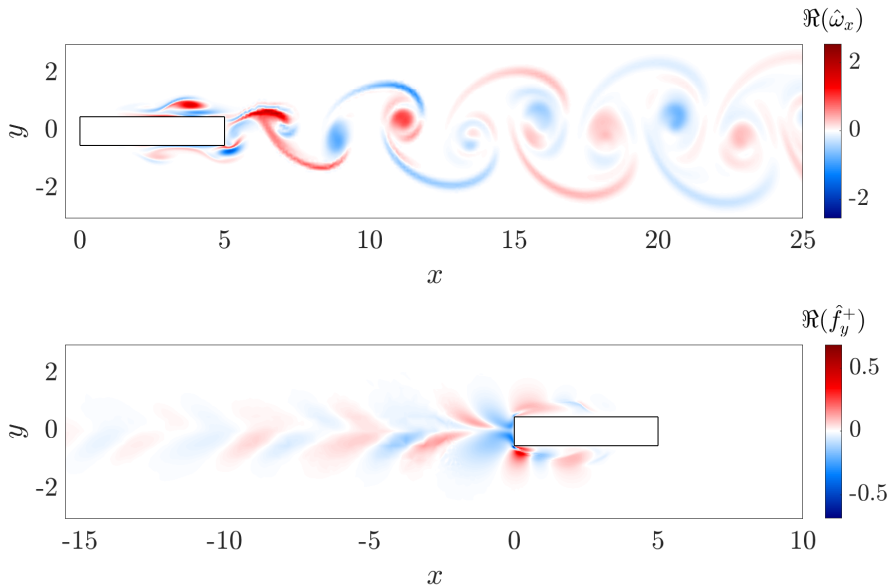should be contrasted with $\Im(\mu) = 0.000816$ of mode QS in the present case. The

Figure 7: Unstable mode for $Re = 550$ and $k = 2.1$. Top: real part of the streamwise vorticity of the direct mode. Bottom: Real part of the $\hat{f}_y^+$ component of the adjoint mode.

different nature of this mode and its triggering mechanism will be illustrated later (see §4.5).

The existence of this pair of unstable Floquet multipliers with negative real part and nearly zero imaginary part is in agreement with the observation by Marques *et al.* (2004) and Blackburn *et al.* (2005), based on the seminal work of Swift & Wiesenfeld (1984), that systems with a spatio-temporal symmetry cannot undergo a period-doubling codimension-one bifurcation. In terms of Floquet analysis, it means that multipliers outside the unit circle can not have negative real part and null imaginary part. This recalls the dispute regarding the nature of the mode QP instability in the wake of a square cylinder. Robichaux *et al.* (1999) reported a subharmonic instability, but Blackburn & Lopez (2003) demonstrated its quasi-periodic nature. Later, Blackburn & Sheard (2010) showed that this mode is subharmonic only when the base flow becomes asymmetric, proving their claim by placing the square cylinder at an incidence of seven degrees with respect to the incoming flow. Following the same reasoning, we have repeated the Floquet analysis at $Re = 500$ using slightly asymmetric boundary conditions at the inlet and at the far field, by enforcing $V = 0$ but $U = U_\infty (1 + \delta y/D)$. A very small $\delta = 1.6 \times 10^{-5}$ is enough for the multipliers to collapse to the real axis, thus yielding a truly subharmonic unstable mode.

4.2. *Direct and adjoint modes*

The top panel in figure 7 shows the spatial structure of the real part of the streamwise vorticity of the unstable QS mode for $Re = 500$ and $k = 2.1$. The perturbation field is maximum near the vortex cores of the base flow, like for the flow past other bluff bodies (see for example Thompson *et al.* 2001; Chaurasia & Thompson 2011). Unlike the square and circular cylinders (Noack & Eckelmann
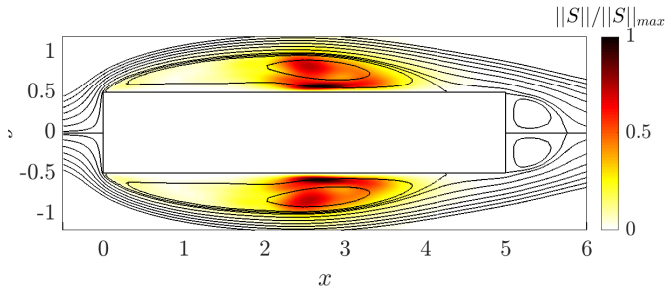
Figure 8: Streamlines and spectral norm of the tensor field S evaluated at $k = 2.1$ and $Re = 550$.

1994; Robichaux *et al.* 1999; Barkley & Henderson 1996), elongated cylinders with elliptic LE (Ryan *et al.* 2005) and the primary instability of the same rectangular cylinders (Chiarini *et al.* 2021*b*), here the perturbation field is not localised in the wake: indeed, large perturbations are observed also over the cylinder side. Hence, the QS mode is not an unstable mode of the wake, but relates to the separating and reattaching flow over the cylinder side and to the vortex splitting/shedding, as it will be discussed later. The symmetry is such that the sign of the streamwise vorticity changes from one period to the next, in agreement with the nearly subharmonic nature of the mode.

The bottom panel of figure 7 shows the spatial structure of the real part of the f_y^+ component of the adjoint mode, which propagates upstream. Large values are observed over the fore portion of the cylinder, with maxima placed near the LE corners, identified as the region of maximum receptivity of the flow. This differs from the primary instability, where the maximum receptivity is found close to the TE corners (Chiarini *et al.* 2021*b*).

4.3. *Structural sensitivity*

Following the work by Giannetti *et al.* (2010), figure 8 plots the spectral norm of the time-averaged structural sensitivity tensor S for $k = 2.1$ at $Re = 550$, with the mean streamlines in the background. We have compared other norms and several values of k and Re, but the map did not change significantly.

The norm $\|S\|$ of the sensitivity tensor vanishes almost everywhere, except near the top/bottom sides of the cylinder, indicating a localised wavemaker region. It differs from the three-dimensional instability of the circular and square cylinders (Giannetti *et al.* 2010) and the primary instability of rectangular cylinders (Chiarini *et al.* 2021*b*), where the sensitivity is always located within the recirculation region downstream the TE, thus suggesting a different triggering mechanism for the present instability. Figure 8 shows four local maxima of the sensitivity norm, two for each side. One maximum of each pair is located very close to the cylinder surface at $x \approx 2.6$ and $y \approx \pm 0.55$. A second, slightly lower maximum is placed at $x \approx 2.56$ and $y \approx \pm 0.8$, very close to the stagnation point at the center of the mean recirculation. Overall, the map of $\|S\|$ confirms the suggestion put forward above that the unstable QS mode does not originate in the wake, and that the triggering mechanism is embedded in the dynamics of the side recirculation, namely in its periodic sequence of enlargement, vortex splitting and shrinking.
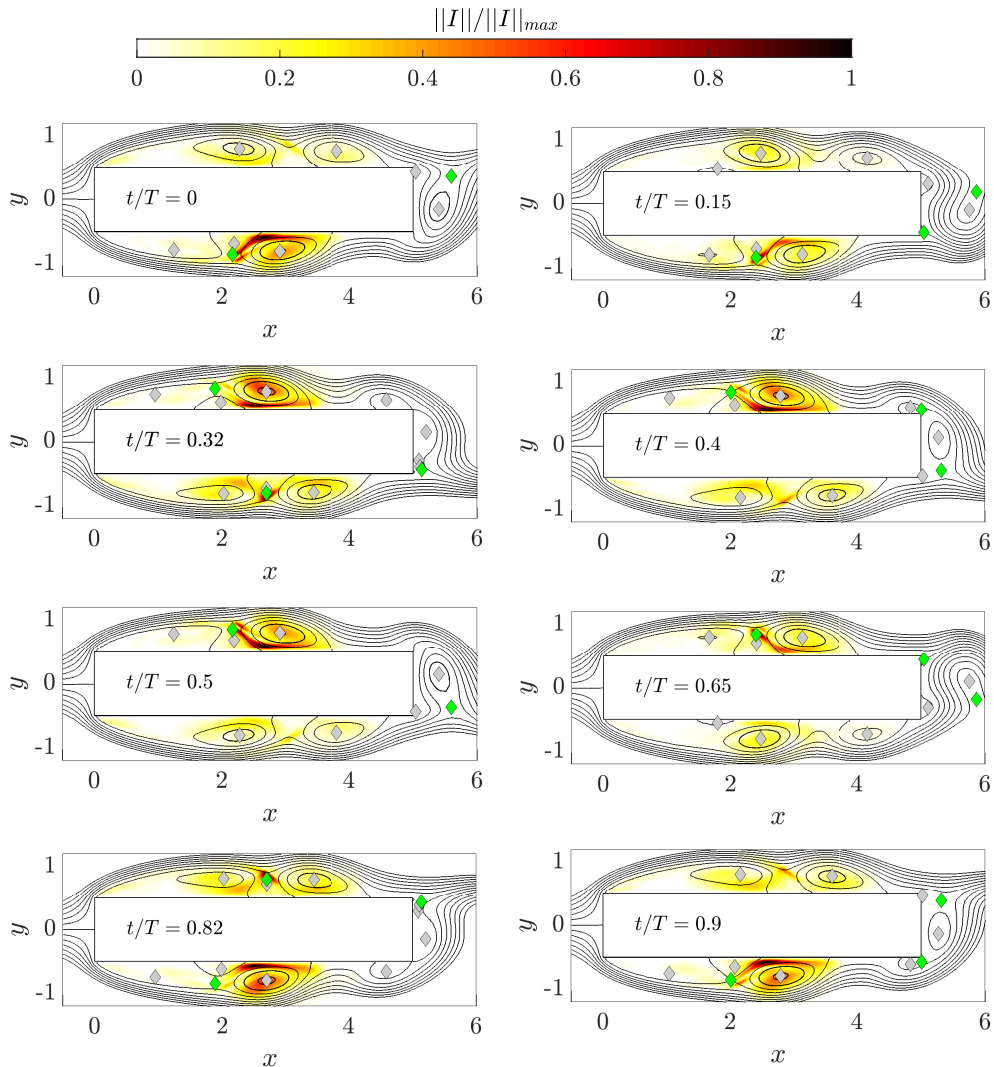
Figure 9: Structural sensitivity for $k = 2.1$ at $Re = 550$. Spectral norm of the tensor field I and streamlines of the base flow at the four times along the shedding cycle. Grey/green diamonds indicate elliptical/hyperbolic stagnation points.

Although the cycle-averaged tensor S locates the core of the three-dimensional instability on the cylinder side, the instantaneous sensitivity tensor I provides further insight, as it describes intra-cycle variations. Since I is the result of the product between the direct and adjoint Floquet modes (see 2.10), it possesses the the same periodicity of the base flow, i.e. $I(x, y, k, t) = I(x, y, k, t + T)$. In figure 9 the norm $\|I\|$ is plotted at eight instants along one shedding cycle. The two pairs of maxima remain localised over the sides of the cylinder during the entire shedding cycle. The first maximum is centred in the hyperbolic stagnation point that separates the side recirculation before the shedding (see the bottom side at $t/T = 0.15$), whereas the second highlights the recirculation region which is about to be shed (see the top side at $t/T = 0.32$). Referring to the top side
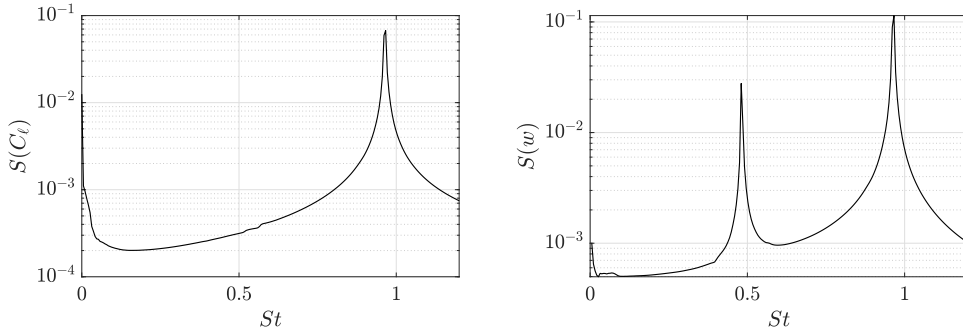
Figure 10: Temporal flow scales extracted by a three-dimensional DNS at $Re = 500$. Power spectrum of the lift coefficient C_ℓ (left) and of the spanwise velocity component w measured at the position $(x, y, z) \approx (7, 0.5, \pi)$ (right).

only, $\|I\|$ becomes first significant at $t/T \approx 0.32$, when the vortex splitting starts and the hyperbolic stagnation point appears. At first, I is mostly localised in the recirculation region identifying the new generated vortex before being shed, with large values in the elliptical stagnation point (i.e. its centre of rotation) and close to the cylinder side where the streamlines have large curvature. Then, in the phases before the vortex is shed, I is mostly relevant in the region close to the hyperbolic stagnation point where the vortex splitting is occurring; see $t/T = 0.65$ and $t/T = 0.82$. When the vortex is eventually shed and the hyperbolic stagnation point disappears, no significant values of I are further observed; see $t/T = 0$ and $t/T = 0.15$. Overall, this indicates that the onset of the three-dimensional instability is embedded in the vortex splitting and in the interaction between the involved recirculation regions, before the LE vortex shedding occurs.

4.4. *Three-dimensional direct numerical simulation*

A three-dimensional direct numerical simulation (DNS) has been performed to confirm and expand the result of the Floquet analysis. The Reynolds number has been set to $Re = 500$, i.e. just above the critical value $Re_{c2} = 480$ predicted by the Floquet analysis. The two-dimensional potential flow solution has been used as initial condition. After having discarded the initial transient, the simulation has been advanced for about 400 shedding cycles with a variable time step to ensure $CFL \leqslant 1$, yielding on average $\Delta t \approx 0.0077 D/U_\infty$.

We start focusing on the temporal flow scales, shown in figure 10 in terms of power spectra against the dimensionless frequency $St = fL/U_\infty$. The left panel shows the power spectrum of the lift coefficient $S(C_\ell)$; in this case the lift coefficient is defined as the vertical component of the aerodynamic force per unit span made dimensionless with $0.5\rho U_\infty^2 D$. The right panel, instead, shows the spectrum of the spanwise velocity component w evaluated at the point with coordinates $(x, y, z) \approx (7, 0.5, \pi)$. The peak in the spectrum of C_ℓ identifies the shedding frequency of the base flow, i.e. $St = 0.966$. This value is nearly coincident with the frequency identified by the two-dimensional simulation, i.e. $St = 0.960$, with a difference of less than 1%. The three-dimensional simulation reveals that the flow is three-dimensional at this Reynolds number, confirming the results of the linear Floquet stability analysis. The power spectrum of w contains two dominant frequencies. The largest one, i.e. $St \approx 0.961$, is associated with the

vortex shedding and coincides with the C_ℓ peak. A second lower peak is found for $St \approx 0.480$, indicating the time scale of the three-dimensional instability and confirming its almost subharmonic nature. Again, this time scale is in excellent agreement with the results of the Floquet analysis. In fact, the unstable pair of Floquet multipliers found for $Re = 500$ at $k = 2.1$ are $\mu = (-1.087 \pm 0.000816)$, corresponding to an unstable mode with frequency $St \approx 0.475$; the difference between the two values is again about 1%. The frequency associated with the unstable QS mode appears in the power spectrum of the signal for the three velocity components recorded in various positions, but it is not visible in the signal of the lift and drag coefficients as, being sinusoidal in the spanwise periodic direction, the contribution of the perturbation on the aerodynamic forces is null.

Figure 11 presents the spatial structure of the three-dimensional unstable mode, visualised through the λ_2 quantity (Jeong *et al.* 1997). Grey surfaces corresponding to $\lambda_2 = -2$ are drawn together with surfaces of positive (red) and negative (blue) streamwise vorticity $\omega_x = \pm 0.25$. Three-dimensional, hairpin-like structures originate from the lift up and stretching of the spanwise-aligned vortices at $x \approx 2.6$, i.e. the position over the cylinder side where the structural sensitivity is largest. The spanwise wavelength of the hairpin vortices, constrained by the spanwise size of the computational domain, is $\lambda = 2\pi/k \approx \pi$ and fits well the result of the Floquet analysis. These structures are then convected in the wake, where they transform into rib-like, streamwise-aligned structures. The field of streamwise vorticity closely resembles the direct mode plotted in figure 7. It is generated over the cylinder side at $x \approx 2.6$ close to the legs of the hairpin structures, and develops in the wake. Its sign changes from one period to the next, in agreement with the almost subharmonic nature of the QS mode.

To further emphasise the quasi subharmonic nature of the three-dimensional QS mode, figure 12 plots isosurfaces of $\lambda_2 = -2$ at the same phase of two consecutive shedding cycles. The hairpin-like structures characterising the instability are the same, but they are spatially shifted by half a period π in the spanwise direction. Sasaki & Kiya (1991), Tenaud *et al.* (2016) and Chaurasia & Thompson (2011) for a blunt flat plate observed a staggered pattern of hairpin-like vortices, denoted as "pattern B". Here, due to the lower aspect ratio, such staggered pattern is not observed: only one line of hairpin vortices appears that is alternately shifted. In fact, when the hairpin vortices are generated, those generated at the previous period have already broken up and convected in the wake. The same pattern of staggered hairpin vortices was observed by Cimarelli *et al.* (2018) and Chiarini & Quadrio (2021) for the same rectangular cylinder with $Æ = 5$ in the turbulent regime at $Re = 3000$. Therefore, the mechanism triggering this three-dimensional instability appears to remain active in the turbulent regime, where the large-scale motions associated with the flow instabilities coexist with the small-scale turbulent fluctuations. This suggest that this three-dimensional instability is involved in the generation of small-scale turbulent structures that, in turn, do not destroy the large coherent structures, as they are detected also in the turbulent flow where they contribute to TKE production (Bernal *et al.* 1979; Browand & Troutt 1980). Hairpin vortices arranged in a staggered manner and with spanwise wavelength $\lambda \approx 3$ have been also observed by Hourigan *et al.* (2001) for more elongated rectangular cylinders with $Æ = 10$ and $Æ = 13$ at $Re = 350 - 400$. This suggests that the QS unstable mode discovered here might be at play even for more elongated cylinders. Furthermore, the lower Reynolds
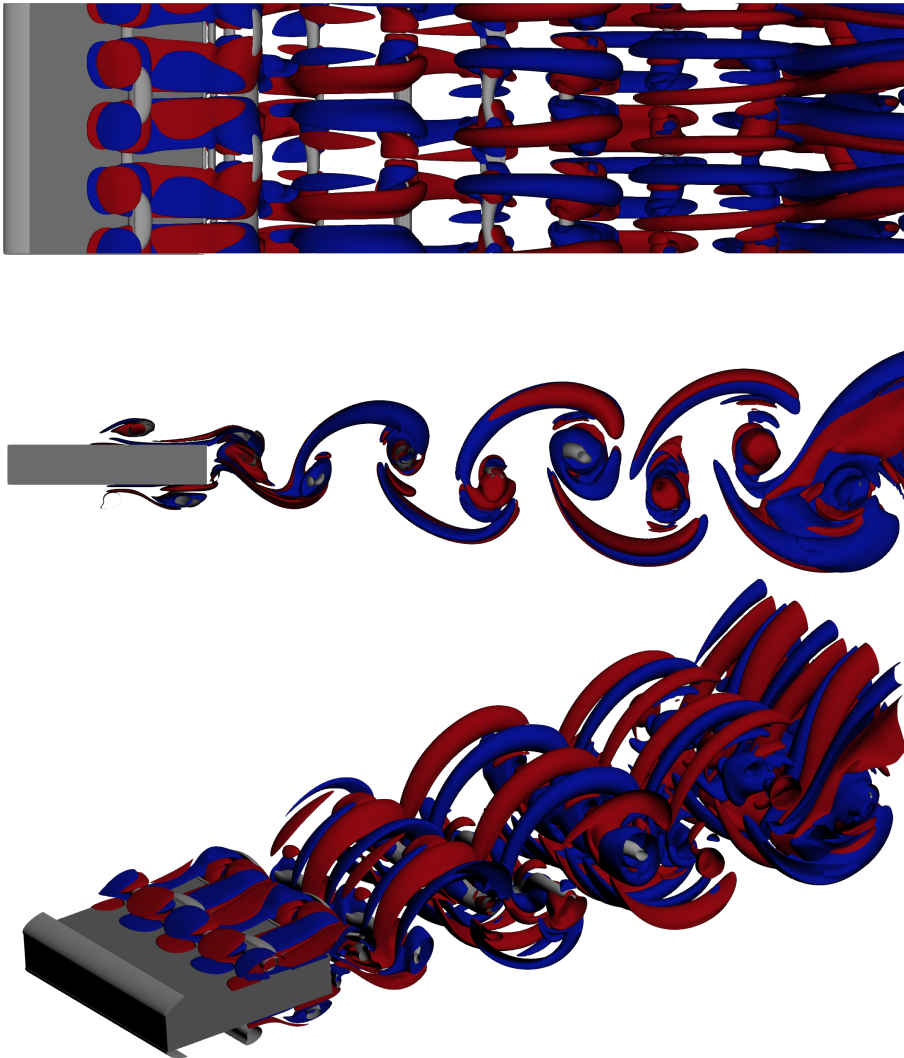
Figure 11: Instantaneous flow visualisation from DNS at $Re = 500$. Grey surfaces indicate $\lambda_2 = -2$. Red and blue surfaces indicate positive and negative streamwise vorticity $\omega_x = \pm 0.25$.

number of their simulations suggests that the critical Reynolds number might slightly decrease with $Ꞑ$.

4.5. *Physical mechanism*

In this section, the physical mechanism responsible for the onset of the three-dimensional instability is investigated. The structural-sensitivity map indicates that the wavemaker is localised over the longitudinal sides of the cylinder. The phase sensitivity tensor I shows that the onset of the instability is associated with the interaction of the two recirculation regions separated by the hyperbolic stagnation point before the downstream vortex is shed. One would be tempted to
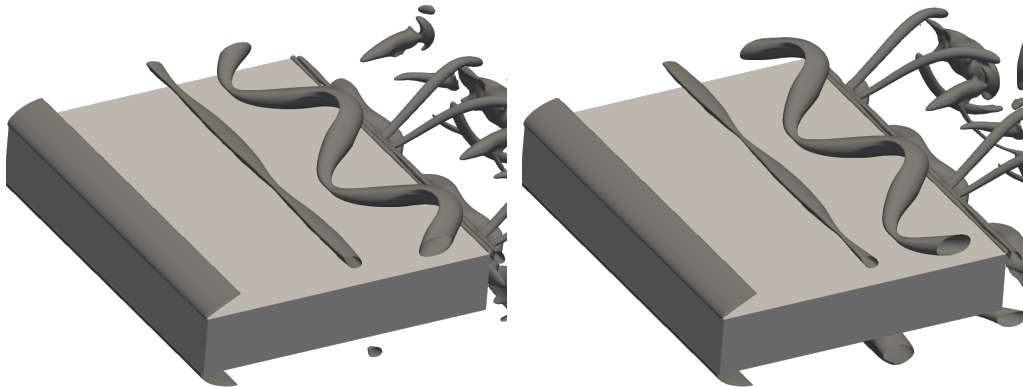
Figure 12: Instantaneous flow visualisation from DNS at $Re = 500$. Isosurfaces of $\lambda_2 = -2$ at the same phase for two consecutive shedding cycles.
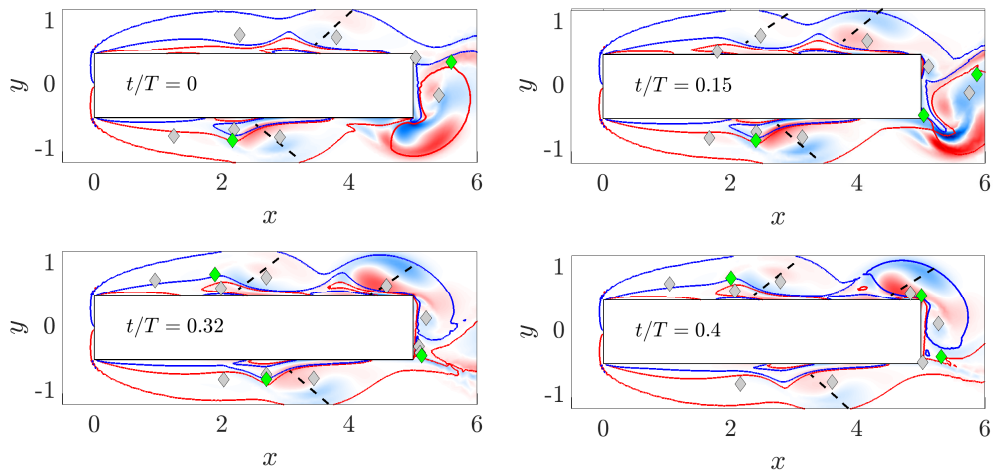

Figure 13: Four instants within half of the shedding period at $Re = 550$. The colormap represents the spanwise vorticity of the unstable mode. Red/blue lines denote values of the base flow spanwise vorticity of $\omega_z = \pm 1$. Grey/green diamonds indicate elliptical/hyperbolic stagnation points. The dashed black lines denote the direction of maximum strain within the base flow vortices.

interpret this as an elliptical instability, with the implication that the transition from two- to three-dimensional flow would be due to a linear mechanism that breaks up singular regions of elliptical streamlines. However, this instability is in fact not elliptic. The discussion below considers the unstable mode for $k = 2.1$ at $Re = 550$, but the general picture is unchanged for other wavenumbers and Re.

Figure 13 considers four phases within one half of the shedding period. Iso-contours of the base flow vorticity are plotted together with the stagnation points and a colormap of the spanwise vorticity of the unstable QS mode. The occurrence of the maximum of the perturbation field in the base-flow vortex cores and the distribution of the spanwise perturbation vorticity may indicate that the instability is elliptical (Kerswell 2002). Indeed, as required for an elliptical instability, the streamlines marking the base flow vortices have an elliptic shape,

with major and minor axes approximately aligned with the x and y direction; see figure 4. Moreover, the spanwise perturbation vorticity shows the two-lobe structure typical of an elliptical instability (Waleffe 1990). The centres of the two lobes are aligned at approximately 45 degrees with respect to the axis of the ellipses (the direction of maximum strain is shown in figure 13 by dashed black lines). Interestingly, these features of the base flow and of the unstable mode closely resemble what found by Chaurasia & Thompson (2011) for a blunt flat plate and, as they conclude, correspond to the required features for an elliptical instability. However, the flow past elongated rectangular cylinders possesses two features which are not consistent with an elliptical instability. The first is the almost subharmonic unstable mode. As shown by Waleffe (1990) and Kerswell (2002), for an unbounded strained vortex with strain rate $\to 0$ the instability is a subharmonic resonance, and has a frequency which is twice that of the elliptical flow. Therefore, the present quasi subharmonic instability would fit the elliptical instability theory if the turnover rate of the base flow vortices was approximately equal to the shedding period $T \approx 5.2$. This is not the case: their rotational rate $\Omega \approx \omega/2$ can be estimated at $2 - 2.5$, which corresponds to a turnover time $\tau \approx 3.1 - 3.5$. The second problem is the lack of this instability for shorter rectangular cylinders with only $n = 1$ LE vortex accommodated over the cylinder side (Chiarini *et al.* 2022). Indeed, we have not detected the QS mode for $3 \leqslant \textit{Æ} < 4.8$, although isolated recirculation regions with elliptical streamlines are present over the cylinder sides.

Hence, we surmise that the transition towards a three-dimensional flow does not result from an elliptical instability of each recirculating region placed over the cylinder sides. The physical mechanism, instead, is purely inviscid and results from the mutual interaction between the vortices. This route was first shown by Pierrehumbert & Widnall (1982) for the family of periodic coherent shear layer vortices introduced by Stuart (1967), based on an exact solution of the two-dimensional Euler equations. They found this configuration of vortices to be unstable to both two-dimensional and three-dimensional subharmonic perturbations, with the former having a larger growth rate. They observed that the three-dimensional unstable mode stretches successive vortices alternately above/below and forward/backward, leading to a configuration which is reminiscent of the pattern of the staggered hairpin vortices discussed above. Pierrehumbert & Widnall (1982) associated this instability to the so-called "helical pairing" seen by Chandrsuda *et al.* (1978). However, in their model the presence of the wall is not accounted for, and the two-dimensional instability dominates with its larger growth rate. Robinson & Saffman (1982) investigated the stability, in the limit of small vortex cross-sectional area and long axial-disturbance wavelength, of different vortex configurations including the one of co-rotating vortices over a slip wall. For this case, they found that the fastest growing disturbances are subharmonic and three-dimensional, with spanwise wavelength approximately twice the distance between two successive vortices L_v (see figure 9 of their paper), which fits very well our observations as $\lambda/L_v \approx 2$. By means of the Taylor frozen flow hypothesis, this spatially subharmonic instability can be easily translated to our spatially evolving case, where the instability is almost subharmonic in time. At lower $\textit{Æ}$, we argue that this instability is not observed because the dynamics of the base flow is quite different (Chiarini *et al.* 2022), and much less time is available for the recirculation regions to interact with each other. An identical mechanism was later proposed by Huang *et al.* (2017) to explain the
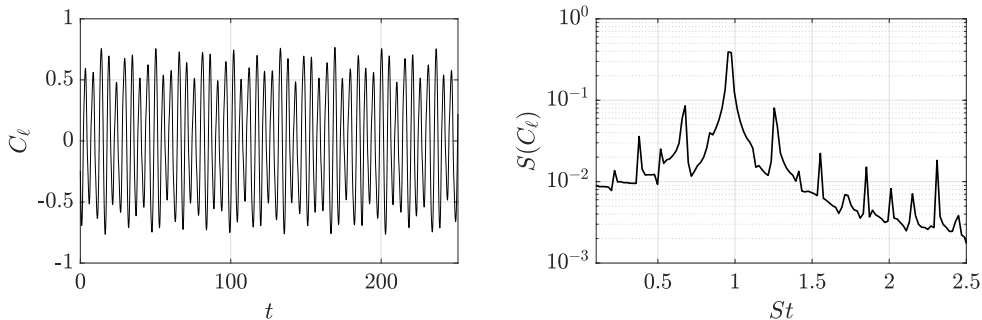
Figure 14: Two-dimensional simulation of the flow past a rectangular cylinder with $\mathit{R} = 5$ at $Re = 600$. Left: time history of the lift coefficient C_ℓ. Right: power spectrum of C_ℓ.

onset of three-dimensionality in the flow over a blunt flat plate; see also Abdalla & Yang (2004). However, the flow past a rectangular cylinder is quite different from that past a blunt flat plate. In fact, for the rectangular cylinder at the present Re, the two-dimensional, periodic base flow is the result of the so-called ILEV instability (Hourigan *et al.* 2001). Due to the interaction of a LE vortex with the TE corner, a pressure pulse arises, travels upstream and triggers the shedding of a new LE vortex, producing a self-sustained mechanism. In the flow over a blunt flat plate, instead, the ILEV instability does not occur, as there is no TE. In this case, the vortices shed from the LE shear layer that foster the three-dimensional instability result from a Kelvin–Helmholtz instability of the shear layer (Chaurasia & Thompson 2011). In the flow past elongated rectangular cylinders, a Kelvin–Helmholtz instability of the LE shear layer is not observed at the Reynolds number here considered, although it becomes a key feature of the flow at larger Re, as described by Chiarini *et al.* (2021*a*) at $Re = 3000$ in the turbulent regime. A further difference between the two flows is that for the blunt flat plate the three-dimensional instability is exactly subharmonic, since the base flow does not satisfy the present spatio-temporal symmetry.

To sum up, we propose that this almost subharmonic instability is triggered by the mutual inviscid interaction of the vortices associated with the recirculation regions coexisting over the cylinder side, separated by a hyperbolic stagnation point before the vortex splitting occurs.

5. A second two-dimensional instability

In this section, the onset of a second, two-dimensional instability for the two-dimensional periodic base flow past a rectangular cylinder with $\mathit{R} = 5$ is described.

When the Reynolds number is increased above $Re \approx 555$, the two-dimensional base flow undergoes a second two-dimensional instability. This is seen in figure 14 where the time history of the lift coefficient C_ℓ is shown (left) for a two dimensional simulation at $Re = 600$, together with its power spectrum (right). Unlike at lower Re, the left panel reveals that the flow is not periodic anymore, with the time history containing more than one frequency. The power spectrum has three main peaks, at $f = 0.13542$, $f = 0.19118$ and $f = 0.25092$, corresponding to $St = 0.677$, $St = 0.9559$ and $St = 1.2546$. The intermediate one is present also at
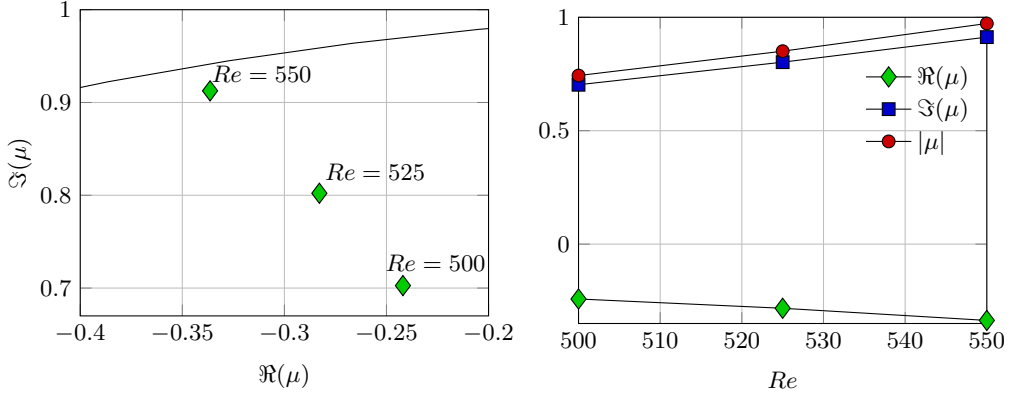
Figure 15: Floquet analysis of the secondary two-dimensional instability of the flow past a rectangular cylinder with $\mathcal{R} = 5$. Left: least stable Floquet multipliers at $Re = 500, 525$ and 550; the continuous line represents the unit circle. Right: dependence of $|\mu|$, $\Re(\mu)$ and $\Im(\mu)$ on Re.

lower Re and is associated with the vortex shedding. The other two peaks, instead, are associated with the onset of the secondary two-dimensional instability.

The onset of this instability has been studied with a two-dimensional Floquet analysis. The same numerical procedure described for the three-dimensional case is used, but here the spanwise wavenumber is $k = 0$.

5.1. *Floquet Multipliers*

Figure 15 shows the evolution of the dominant Floquet multipliers for Reynolds numbers in the range $500 \leqslant Re \leqslant 550$. The branch corresponds to a pair of complex conjugate multipliers with negative real part and relatively large imaginary part. Increasing the Reynolds number, $|\mu|$ nears the unit circle: at $Re = 550$ it is $\mu \approx (-0.336, \pm0.912)$ corresponding to $|\mu| \approx 0.973$, indicating that $Re = 550$ is slightly lower than the critical Reynolds number of this instability. The right panel of figure 15 shows that, by increasing Re, both $|\mu|$ and $\Im(\mu)$ increase while $\Re(\mu)$ slightly decreases. The frequency associated with this complex conjugate pair is fully consistent with the peaks found in the spectrum for $Re = 600$ in figure 14. Indeed, with the Floquet analysis the perturbation field may be written as:

$$\begin{aligned}
\boldsymbol{u}(x,y,t) &= \hat{\boldsymbol{u}}(x,y,t)\mathrm{e}^{\sigma t}, \\
p(x,y,t) &= \hat{p}(x,y,t)\mathrm{e}^{\sigma t},
\end{aligned} \tag{5.1}$$

where $\{\hat{\boldsymbol{u}}, \hat{p}\}$ is the two-dimensional Floquet mode with period T and σ is the eigenvalue associated with μ

$$\sigma = \frac{1}{T}\log(\mu). \tag{5.2}$$

At $Re = 550$ (the closest to criticality), the Floquet exponents associated with this mode are $\sigma = (-0.0053, \pm0.3682)$. Therefore the $\{\boldsymbol{u}, p\}$ perturbation field is characterised by a frequency of $f_T \pm f_{2D}$ — where $f_T = 0.1914$ indicates the shedding frequency and $f_{2D} = \Im(\sigma)/2\pi$ — that corresponds to $f = 0.1328$ and $f = 0.2500$ (or $St = 0.6640$ and $St = 1.25$) which are very close to the values found in the spectrum of C_ℓ at $Re = 600$ (see the right panel of figure 14).
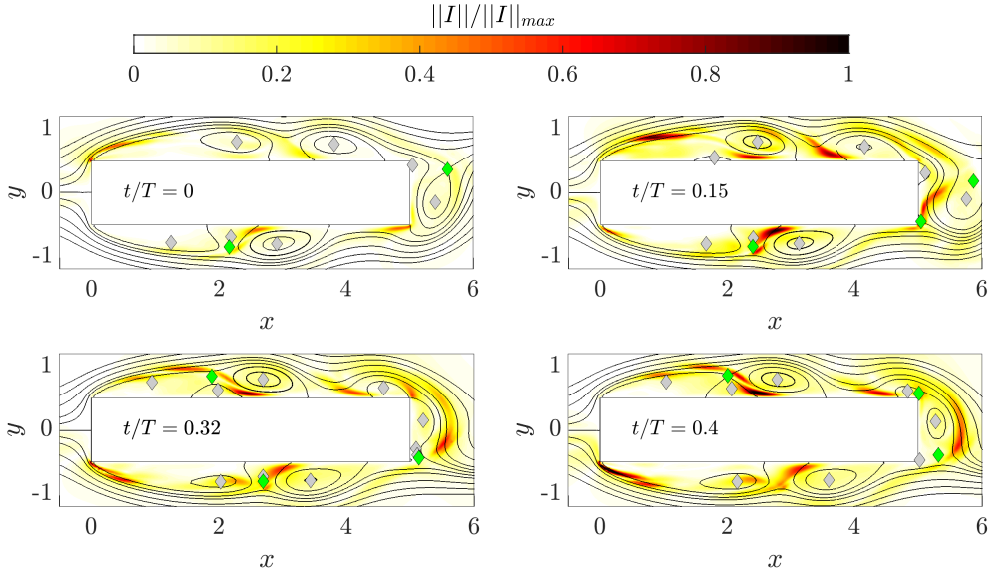
Figure 16: Structural sensitivity of the second two-dimensional instability at $Re = 550$. Spectral norm of the tensor field I and streamlines of the base flow at four times along the shedding cycle. Grey/green diamonds indicate elliptical/hyperbolic stagnation points.

From the values of these Floquet multipliers at different Re one can extrapolate the critical Reynolds number of the onset of this instability, i.e. Re_{c3}, as the Re at which μ crosses the unit circle. By using a second order extrapolation we found $Re_{c3} \approx 555$.

5.2. *Structural sensitivity*

Figure 16 plots the instantaneous sensitivity at four times within half of the shedding period, i.e. $t/T = 0, 0.15, 0.32$ and 0.4. As for the three-dimensional case, the sensitivity indicates that the wavemaker is localised close to the cylinder, and goes to zero both upstream and downstream. At all times, the largest sensitivity is where the streamlines have large curvature. For a more detailed description we focus on the upper side of the cylinder. In the first panel, corresponding to $t/T = 0$, a large sensitivity is observed near the LE corner, suggesting a link to the Kelvin–Helmholtz instability of the separated shear layer. At larger t/T, the largest values are shifted within the separated shear layer and in the main recirculating region close to the cylinder side, in the reverse boundary layer just before the separation point (see the top right panel). At even larger t/T, the structural sensitivity further highlights the second region, indicating its relevance in the onset of the instability, until the vortex splitting occurs (see the top region of the flow in the bottom panels). Lastly, at $t/T = 0.4$ the largest sensitivity is in the upstream part of the newly formed vortex shed downstream, close to the cylinder vertical side.

6. Conclusions

The three-dimensional instability of the flow past a rectangular cylinder has been studied with Floquet analysis and direct numerical simulations. The aspect ratio $Æ$ of the cylinder is $Æ = 5$, a value which defines the international Benchmark of the Aerodynamics of a Rectangular 5:1 Cylinder, or BARC.

The Floquet analysis has brought to light a new quasi-subharmonic (QS) unstable mode, so far undetected for other bluff bodies. A true codimension-one subharmonic mode cannot exist owing to the symmetries governing the base flow (Blackburn & Lopez 2003; Marques *et al.* 2004; Blackburn *et al.* 2005). However, a very small flow asymmetry is observed to lead to a truly subharmonic mode. The Reynolds number at which the QS mode first becomes unstable is $Re_{c,2} \approx 480$, and its wavelength is $\lambda = 2\pi/k \approx 3$. Unlike the unstable modes of the flow past circular cylinders (Barkley & Henderson 1996), short rectangular cylinders (Choi & Yang 2014; Blackburn & Sheard 2010) and elongated cylinders without vortex shedding from the LE (Ryan *et al.* 2005), this is not an unstable mode of the wake: in fact its perturbation field develops upstream of the TE, over the cylinder side. This suggests that the scenario for three-dimensional instabilities valid for short rectangular and circular cylinders and for elongated cylinders with smooth leading edges cannot be generalised to every time-periodic flow past two dimensional bluff bodies, even when the flow possesses a reflection symmetry with respect to the wake centreline.

The structural sensitivity has shown that the wavemaker of the QS mode is localised over the cylinder side. A detailed inspection of the instantaneous sensitivity has connected the triggering process to the interaction between the two recirculating regions that coexist over the cylinder side before the LE vortex shedding. We have also provided an interpretation of the physical mechanism that triggers this unstable mode: despite some clues, an elliptical instability would be consistent neither with an almost subharmonic mode, nor with its absence at lower $Æ$, where isolated elliptically shaped streamlines over the cylinder side still exist. Our conclusion therefore is that this instability is triggered by the mutual inviscid interaction of the two recirculating regions simultaneously present over the cylinder side at a given time. This mechanism, first proposed by Pierrehumbert & Widnall (1982) and Robinson & Saffman (1982), leads to an unstable almost subharmonic three-dimensional mode, and is fully consistent with the present results. The same triggering mechanism is responsible for the transition to three-dimensionality in the flow over a blunt flat plate. In this case, however, the three-dimensional instability of the Kelvin–Helmholtz vortices shed from the leading edge is exactly subharmonic (Chaurasia & Thompson 2011; Huang *et al.* 2017), since the base flow does not satisfy the spatio-temporal symmetry.

Declaration of Interests

The authors report no conflict of interest.

REFERENCES

ABDALLA, I. E. & YANG, Z. 2004 Numerical study of the instability mechanism in transitional separating–reattaching flow. *Int. J. Heat Fluid Flow* **25** (4), 593–605.

BARKLEY, D. & HENDERSON, R.D. 1996 Three-dimensional Floquet stability analysis of the wake of a circular cylinder. *J. Fluid Mech.* **322**, 215–241.

BERNAL, L. P., BREIDENTHAL, R. E., BROWN, G. L., KONRAD, J. H. & ROSHKO, A. 1979 On the development of three dimensional small scales in turbulent mixing layers. In *2nd Symposium on Turbulent Shear Flows*, pp. 8.1–8.6.

BLACKBURN, H. M. & LOPEZ, J. M. 2003 On three-dimensional quasiperiodic Floquet instabilities of two-dimensional bluff body wakes. *Phys. Fluids* **15** (8), L57–L60.

BLACKBURN, H. M., MARQUES, F. & LOPEZ, J. M. 2005 Symmetry breaking of two-dimensional time-periodic wakes. *J. Fluid Mech.* **522**, 395–411.

BLACKBURN, H. M. & SHEARD, G. J. 2010 On quasiperiodic and subharmonic Floquet wake instabilities. *Phys. Fluids* **22** (3), 031701.

BOGHOSIAN, M. E. & CASSEL, K. W. 2016 On the origins of vortex shedding in two-dimensional incompressible flows. *Theor. Comput. Fluid Dyn.* **30** (6), 511–527.

BREZZI, F. 1974 On the existence, uniqueness and approximation of saddle-point problems arising from lagrangian multipliers. *Esaim. Math. Model Numer. Anal.* **8** (R2), 129–151.

BROWAND, F. K. & TROUTT, T. R. 1980 A note on spanwise structure in the two-dimensional mixing layer. *J. Fluid Mech.* **97** (4), 771–781.

CHANDRSUDA, C., MEHTA, R. D., WEIR, A. D. & BRADSHAW, P. 1978 Effect of free-stream turbulence on large structure in turbulent mixing layers. *J. Fluid Mech.* **85** (4), 693–704.

CHAURASIA, H.K. & THOMPSON, M.C. 2011 Three-dimensional instabilities in the boundary-layer flow over a long rectangular plate. *J. Fluid Mech.* **681**, 411–433.

CHIARINI, A., GATTI, D., CIMARELLI, A. & QUADRIO, M. 2021*a* Structure of turbulence in the flow around a rectangular cylinder. *J . Fluid Mech.* **Submitted**, 1–26.

CHIARINI, A. & QUADRIO, M. 2021 The Turbulent Flow over the BARC Rectangular Cylinder: A DNS Study. *Flow Turbul. Combust.* **107**, 875–899.

CHIARINI, A., QUADRIO, M. & AUTERI, F. 2021*b* Linear stability of the steady flow past rectangular cylinders. *J. Fluid Mech.* **929**, A36.

CHIARINI, A., QUADRIO, M. & AUTERI, F. 2022 On the frequency selection mechanism of the low-Re flow around rectangular cylinders. *J. Fluid Mech.* **933**.

CHOI, C.-B. & YANG, K.-S. 2014 Three-dimensional instability in flow past a rectangular cylinder ranging from a normal flat plate to a square cylinder. *Phys. Fluids* **26** (6), 061702.

CIMARELLI, A., LEONFORTE, A. & ANGELI, D. 2018 On the structure of the self-sustaining cycle in separating and reattacching flows. *J. Fluid Mech.* **857**, 907–936.

CITRO, V., LUCHINI, P., GIANNETTI, F. & AUTERI, F. 2017 Efficient stabilization and acceleration of numerical simulation of fluid flows by residual recombination. *J. Comp. Phys.* **344**, 234–246.

GIANNETTI, F., CAMARRI, S. & LUCHINI, P. 2010 Structural sensitivity of the secondary instability in the wake of a circular cylinder. *J. Fluid Mech.* **651**, 319–337.

GIANNETTI, F. & LUCHINI, P. 2007 Structural sensitivity of the first instability of the cylinder wake. *J. Fluid Mech.* **581**, 167–197.

HECHT, F. 2012 New development in FreeFem++. *J. Num. Math.* **20** (3-4), 251–266.

HOURIGAN, K., THOMPSON, M. C. & TAN, B. T. 2001 Self-sustained oscillations in flows around long blunt plates. *J. Fluids Struct.* **15** (3), 387–398.

HUANG, Y., ZHOU, B., TANG, Z. & ZHANG, F. 2017 Transition scenario and transition control of the flow over a semi-infinite square leading-edge plate. *Phys. Fluids* **29** (7), 074105.

JALLAS, D., MARQUET, O. & FABRE, D. 2017 Linear and nonlinear perturbation analysis of the symmetry breaking in time-periodic propulsive wakes. *Phys. Rev. E* **95** (6-1), 063111.

JEONG, J., HUSSAIN, F., SCHOPPA, W. & KIM, J. 1997 Coherent structures near the wall in a turbulent channel flow. *J. Fluid Mech.* **332**, 185–214.

JIANG, H. & CHENG, L. 2018 Hydrodynamic characteristics of flow past a square cylinder at moderate Reynolds numbers. *Phys. Fluids* **30** (10), 104107.

JIANG, H., CHENG, L. & AN, H. 2018 Three-dimensional wake transition of a square cylinder. *J. Fluid Mech.* **842**, 102–127.

KERSWELL, R. R. 2002 Elliptical Instability. *Annu. Rev. Fluid Mech.* **34** (1), 83–113.

LUCHINI, P. 2013 Linearized no-slip boundary conditions at a rough surface. *J. Fluid Mech.* **737**, 349–367.

LUCHINI, P. 2016 Immersed-boundary simulation of turbulent flow past a sinusoidally undulated river bottom. *Eur. J. Mech. B Fluids* **55**, 340–347.

MARQUES, F., LOPEZ, J. M. & BLACKBURN, H. M. 2004 Bifurcations in systems with Z2 spatio-temporal and O(2) spatial symmetry. *Phys. D: Nonlinear Phenom.* **189** (3), 247–276.

MILLS, R., SHERIDAN, J. & HOURIGAN, K. 2002 Response of base suction and vortex shedding from rectangular prisms to transverse forcing. *J. Fluid Mech.* **461**, 25–49.

MILLS, R., SHERIDAN, J., HOURIGAN, K. & WELSH, M. C. 1995 The mechanism controlling vortex shedding from rectangular bluff bodies. *Proceeding Twelfth Australas. Fluid Mech. Conf.* pp. 227–230.

MONKEWITZ, P. A., HUERRE, P. & CHOMAZ, J.-M. 1993 Global linear stability analysis of weakly non-parallel shear flows. *J. Fluid Mech.* **251**, 1–20.

MOORE, D. M., LETCHFORD, C. W. & AMITAY, M. 2019 Energetic scales in a bluff body shear layer. *J. Fluid Mech.* **875**, 543–575.

NAKAMURA, Y., OHYA, Y. & TSURUTA, H. 1991 Experiments on vortex shedding from flat plates with square leading and trailing edges. *J. Fluid Mech.* **222**, 437–447.

NOACK, B. R. & ECKELMANN, H. 1994 A global stability analysis of the steady and periodic cylinder wake. *J. Fluid Mech.* **270**, 297–330.

OKAJIMA, A. 1982 Strouhal numbers of rectangular cylinders. *J. Fluid Mech.* **123**, 379–398.

OZONO, S., OHYA, Y., NAKAMURA, Y. & NAKAYAMA, R. 1992 Stepwise increase in the Strouhal number for flows around flat plates. *Int. J. Numer. Methods Fluids* **15** (9), 1025–1036.

PARK, D. & YANG, K.-S. 2016 Flow instabilities in the wake of a rounded square cylinder. *J. Fluid Mech.* **793**, 915–932.

PIERREHUMBERT, R. T. & WIDNALL, S. E. 1982 The two- and three-dimensional instabilities of a spatially periodic shear layer. *J. Fluid Mech.* **114**, 59–82.

RAI, M.M. & MOIN, P. 1991 Direct simulations of turbulent flow using finite-difference schemes. *J. Comput. Phys.* **96**, 15.

ROBICHAUX, J., BALACHANDAR, S. & VANKA, S. P. 1999 Three-dimensional Floquet instability of the wake of square cylinder. *Phys. Fluids* **11** (3), 560–578.

ROBINSON, A. C. & SAFFMAN, P. G. 1982 Three-dimensional stability of vortex arrays. *J. Fluid Mech.* **125**, 411–427.

RYAN, K., THOMPSON, M. C. & HOURIGAN, K. 2005 Three-dimensional transition in the wake of bluff elongated cylinders. *J. Fluid Mech.* **538**, 1–29.

SAAD, Y 2011 *Numerical Methods for Large Eigenvalue Problems*. Philadelphia: Society for Industrial and Applied Mathematics.

SAHA, A.K., MURALIDHAR, K. & BISWAS, G. 2000 Transition and chaos in two-dimensional flow past a square cylinder. *J. Eng. Mech.* **126** (5), 523–532.

SASAKI, K. & KIYA, M. 1991 Three-dimensional vortex structure in a leading-edge separation bubble at moderate Reynolds numbers. *J. Fluids Eng.* **113** (3), 405–410.

SHEARD, G. J. 2011 Wake stability features behind a square cylinder: Focus on small incidence angles. *J. Fluids Struct.* **27** (5), 734–742.

SHEARD, G. J., FITZGERALD, M. J. & RYAN, K. 2009 Cylinders with square cross-section: Wake instabilities with incidence angle variation. *J. Fluid Mech.* **630**, 43–69.

SOHANKAR, A., NORBERG, C. & DAVIDSON, L. 1999 Simulation of three-dimensional flow around a square cylinder at moderate Reynolds numbers. *Phys. Fluids* **11** (2), 288–306.

STUART, J. T. 1967 On finite amplitude oscillations in laminar mixing layers. *J. Fluid Mech.* **29** (3), 417–440.

SWIFT, J. W. & WIESENFELD, K. 1984 Suppression of Period Doubling in Symmetric Systems. *Phys. Rev. Lett.* **52** (9), 705–708.

TAN, B. T., THOMPSON, M. C. & HOURIGAN, K. 2004 Flow past rectangular cylinders: Receptivity to transverse forcing. *J. Fluid Mech.* **515**, 33–62.

TENAUD, C., PODVIN, B., FRAIGNEAU, Y. & DARU, V. 2016 On wall pressure fluctuations and

26 *A. Chiarini, M. Quadrio and F. Auteri*

their coupling with vortex dynamics in a separated – reattached turbulent flow over a blunt flat plate. *Intl J. Heat Fluid Flow* **61** (Part B), 730–748.

THOMPSON, M. C., HOURIGAN, K., RYAN, K. & SHEARD, G. J. 2006 Wake transition of two-dimensional cylinders and axisymmetric bluff bodies. *J. Fluids Struct.* **22** (6), 793–806.

THOMPSON, M. C., LEWEKE, T. & WILLIAMSON, C. H. K. 2001 The physical mechanism of transition in bluff body wakes. *J. Fluids Struct.* **15** (3), 607–616.

WALEFFE, F. 1990 On the three-dimensional instability of strained vortices. *Phys. Fluids A: Fluid Dyn.* **2** (1), 76–80.

WILLIAMSON, C. H. K. & GOVARDHAN, R. 2008 A brief review of recent results in vortex-induced vibrations. *J. Wind Eng. Ind. Aerodyn.* **96** (6), 713–735.

Appendix A. Sensitivity of the results to domain size and grid resolution

In this Appendix the dependence of the results on the domain size and grid resolution is addressed. The complete Floquet analysis for $Re = 500$ and $k = 2.1$ is repeated, by varying the extent of the computational domain and the spatial resolution. In the first case the size of the domain is increased in the stream-wise and cross-stream directions from $(L_x, L_y) = (75D, 40D)$ up to $(L_x, L_y) = (100D, 80D)$, while the same grid resolution is adopted. In the second case the size of the domain is kept constant, but the number of elements is increased by about 60%, mainly increasing the resolution near the cylinder and in the wake region. The simulation with increased grid resolution predicts a shedding period within 0.19% the value predicted by the coarser grid, while the pair of complex conjugate Floquet multipliers associated with the detected unstable mode vary from $(-1.087, \pm0.000816)$ to $(-1.024, \pm0.000398)$, corresponding to a variation of $|\mu|$ within 5.5%. The simulation with the larger computational domain, instead, predicts a shedding period within 0.26% of the value predicted with the smaller domain, while the unstable Floquet multipliers are $(-1.047, \pm0.000522)$ corresponding to a variation of $|\mu|$ within 3.7%. However, the almost subharmonic nature of the unstable mode and the physical mechanism responsible for its onset are well described by all the considered grids.

To further consider the influence of the blockage on the unstable mode, two additional simulations are also carried out by decreasing and increasing the size of the domain in the cross-stream direction from $L_y = 40D$ to $L_y = 30D$ and $L_y = 120$; they correspond to a blockage of 3.5% and 0.8% respectively. For both cases, the same spatial resolution adopted in the regular grid is used near the cylinder. For the larger and smaller blockages, the predicted shedding period is respectively within 0.51% and 0.08% the value predicted by the regular grid. The Floquet multipliers associated with the unstable mode, instead, are $\mu = (-1.035, \pm0.00050)$ for $L_y = 40D$ and $\mu = (-1.009, \pm0.000375)$ for $L_y = 120D$, corresponding to a variation of $|\mu|$ that is within 4.7% and 7.1% the value predicted by the regular grid.

The dependence of the three-dimensional simulation on the the grid resolution is addressed by running an additional simulation on a coarser grid with $Nx = 674$, $Ny = 489$ and $Nz = 150$. In this case the frequency associated with the vortex shedding is $St \approx 0.965$, while that associated with the three-dimensional instability is $St \approx 0.482$. Compared to the finer grid, this corresponds to a variation of approximately 0.4% and 0.53%.